Atmos. Chem. Phys., 26, 12197–12210, 2026
https://doi.org/10.5194/acp-26-12197-2026

Atmospheric Chemistry and Physics
Open Access
EGU

Research article

Contrasting nighttime heterogeneous and daytime photochemical aging drive the optical evolution of black carbon

Yin Zhang[1,2], Jinghao Zhai[1,3], Yaling Zeng[1,2], Shao Shi[1,2], Baohua Cai[1,2], Ke Yang[1,2], Yu Yan[1,2], Xin Yuan[1,2], Tianlong Hu[1,2], Chen Wang[1,2], Tzung-May Fu[1,2], Lei Zhu[1,2], Huizhong Shen[1,2], Jianhuai Ye[1,2], and Xin Yang[1,2]

[1]Shenzhen Key Laboratory of Precision Measurement and Early Warning Technology for Urban Environmental Health Risks, School of Environmental Science and Engineering, Southern University of Science and Technology, Shenzhen 518055, China
[2]Guangdong Provincial Field Observation and Research Station for Coastal Atmosphere and Climate of the Greater Bay Area, Southern University of Science and Technology, Shenzhen, Guangdong, 518055, China
[3]Department of Geophysical Sciences, University of Chicago, Chicago 60637, IL, United States

Correspondence: Jinghao Zhai (jinghao@uchicago.edu) and Xin Yang (yangx@sustech.edu.cn)

Received: 1 April 2026 – Discussion started: 27 April 2026
Revised: 23 July 2026 – Accepted: 14 August 2026 – Published: 28 August 2026

Abstract. Black carbon (BC) particles play a critical role in the climate system, yet their atmospheric aging processes and consequent optical impacts in real-world atmospheres remain insufficiently understood. In this study, we present integrated single-particle measurements using a single particle soot photometer (SP2) and a single-particle aerosol mass spectrometer (SPAMS) during a field campaign in urban Shenzhen, China. The mean refractory BC (rBC) mass concentration during the sampling period was 1.2 $\mu g\,m^{-3}$, with core mass median diameters (MMD) of 155–170 nm. The diurnal variation in the coating-to-core mass ratio (MR) indicated that BC underwent continuous aging. Nighttime aging was associated with enhanced nitrate signals and coating growth, potentially influenced by gas–particle partitioning, condensation, and coagulation. Daytime photochemical aging was characterized by rapid nitrate accumulation followed by increases in sulfate and oxidized organic species. Despite their distinct mechanisms, both aging pathways significantly elevated the MR and produced similar net enhancements in the mass absorption cross section (MAC) at 532 nm with an overnight increase of $\sim 0.8\,m^2\,g^{-1}$ and a daytime increase of $\sim 1.0\,m^2\,g^{-1}$. These comparable net increments were primarily due to the offsetting effect of intensive fresh emissions during the day. Specifically, the apparent rates of change in the MAC of core–shell-like BC driven by nighttime heterogeneous reactions and daytime photochemical aging were determined to be 0.36 ± 0.05 and $0.51 \pm 0.11\,m^2\,g^{-1}\,h^{-1}$, respectively. This study provides observationally constrained insights into the contrasting diurnal evolution of BC mixing state and optical properties and quantifies the campaign-specific apparent MAC enhancement rates under urban atmospheric conditions.

Published by Copernicus Publications on behalf of the European Geosciences Union.

1 Introduction

Black carbon (BC), formed during the incomplete combustion of fossil fuels and biomass, represents a major constituent of fine particulate matter in the atmosphere (Bond and Bergstrom, 2006). Its role in both climate systems (Bond et al., 2013) and public health (Baumgartner et al., 2014) is increasingly recognized, as BC contributes substantially to radiative forcing and adverse health outcomes. Owing to its strong light absorption across the solar spectrum, BC is regarded as a potent warming agent in the atmosphere (Jacobson, 2001).

Throughout its atmospheric lifetime, BC undergoes dynamic physical and chemical transformations (Wang et al., 2021a). Numerous studies have investigated changes in BC properties (Zhang et al., 2018; Sun et al., 2020; Popovicheva et al., 2025), and the mechanisms driving its transformation during aging (Gong et al., 2016; Li et al., 2019). Freshly emitted BC typically exhibits a fractal, chain-like aggregate structure (Wang et al., 2021a; Wu et al., 2018). As aging proceeds, the infilling of material within the BC pores can lead to structural collapse and the formation of more compact, near-spherical particles. Continued exposure to atmospheric constituents promote the accumulation of inorganic and organic coatings, ultimately yielding core-shell structures (Riemer et al., 2010; Zhang et al., 2008). This progressive structural and chemical evolution fundamentally dictates the dynamic changes in BC optical properties, leading to enhanced light absorption (Cappa et al., 2012; Bond and Bergstrom, 2006; Fuller et al., 1999; Peng et al., 2016).

However, quantifying the impact of atmospheric aging on BC optical properties in real-world conditions remains challenging. In the ambient, BC particles are subject to the simultaneous influences of emissions, chemical transformation, transport, and removal processes. While optical models and controlled chamber experiments often predict substantial absorption enhancement for heavily coated BC, field observations frequently report much weaker enhancements, even at high MR (Cappa et al., 2012, 2019). A compelling explanation for this discrepancy is the complex heterogeneity of BC mixing state in real-world environments (Fierce et al., 2016; Zhai et al., 2022a). Meteorological variations and emissions also constantly alter the population heterogeneity of BC particles at a given site. This dynamic interplay significantly complicates the bulk optical response, often causing the actual absorption enhancement to fall short of theoretical expectations derived from homogeneously mixed assumptions.

While field observations typically capture bulk BC mixture of ambient BC that is difficult to differentiate, advanced instrumentation enables detailed characterization of individual particle properties. A suite of instruments has been developed for this purpose (Petzold et al., 2013), among which the single particle soot photometer (SP2) is widely used for real-time measurements of BC mass and mixing state at the single-particle level (Stephens et al., 2003; Schwarz et al., 2006; Sedlacek et al., 2012). Complementing the physical information provided by the SP2, the soot particle aerosol mass spectrometer (SP-AMS) is utilized to characterize the chemical composition of BC-containing particles. Joint deployments of SP2 and SP-AMS have yielded high-resolution insights into BC mixing states and chemistry (Liu et al., 2014; Cappa et al., 2012, 2019). The single particle aerosol mass spectrometer (SPAMS, distinct from SP-AMS), provides real-time chemical characterization of individual particles (Zhai et al., 2022a, b). Compared with SP-AMS, which primarily measures ensemble composition, SPAMS resolves particle-to-particle heterogeneity and identifies chemical tracers critical for source apportionment. Gong et al. (2016) demonstrated that SP2 and SPAMS, when used together, can effectively capture rapid changes in BC coatings during pollution events. Despite the strong complementarity of these instruments, joint field deployments remain rare, leaving an observational gap.

In this study, we analyzed observational data collected during a period minimally influenced by long-range transport and dominated by local traffic emissions in Shenzhen, China, a coastal megacity exhibits a distinctive combination of emission sources and meteorological conditions typical of subtropical urban environments. The region is characterized by strong atmospheric oxidative capacity, where abundant precursors from intensive vehicular traffic drive vigorous photochemical activity (Xue et al., 2016). By integrating SP2 and SPAMS measurements, we resolved the diurnal aging behavior of freshly emitted BC particles and identified the associated chemical processes governing their evolution. When combined with concurrent optical measurements, these observations enabled quantification of the rates of optical change induced by both nighttime heterogeneous processing and daytime photochemical aging. This research provides direct observational evidence that tracks the diurnal aging pathways of BC under real urban atmospheric conditions, quantifying the subsequent rate of optical enhancement.

2 Methods

2.1 Field Measurements

Field measurements were carried out at the Southern University of Science and Technology (22°32′ N, 114°03′ E) in Shenzhen, China, from 21 November to 10 December 2021. Situated in the urban core, the sampling site provides a representative profile of aerosol characteristics typical of densely populated regions within the Pearl River Delta (PRD).

Ambient aerosols were drawn through a diffusion drying prior to instrument sampling to minimize the influence of ambient humidity. Refractory black carbon (rBC) was characterized at the single-particle level using a SP2 (Droplet Measurement Technologies, Boulder, CO, USA). To obtain complementary chemical composition information for indi-

vidual particles, a SPAMS (Hexin Analytical Instrument Co., Ltd., Guangdong, China) was deployed alongside the SP2. In parallel, a photoacoustic extinctiometer (PAX; Droplet Measurement Technologies, USA), operating at a wavelength of 532 nm, was used to quantify the bulk optical properties of the collected aerosols. To maintain data accuracy and minimize potential instrumental drift during continuous sampling, routine calibrations and performance checks were conducted throughout the campaign.

Simultaneous measurements of gaseous pollutants (O_3, NO, NO_2, NO_x, and CO) and particulate matter ($PM_{2.5}$) were conducted at the site, together with meteorological parameters including temperature, relative humidity, wind speed, and wind direction. The mixing layer height (MLH) was obtained from the ERA5 hourly reanalysis dataset provided by the European Centre for Medium-Range Weather Forecasts (ECMWF). ERA5 data were retrieved at a horizontal resolution of $0.25° \times 0.25°$. The time series of MLH for the sampling site was extracted using the nearest-neighbor interpolation method. To assess the influence of regional air mass transport, 72 h backward trajectory analyses were performed using the HYSPLIT-4 model (Hybrid Single-Particle Lagrangian Integrated Trajectory), developed by the Air Resources Laboratory (ARL) of the U.S. National Oceanic and Atmospheric Administration (NOAA), with arrival heights set at 100 m a.g.l. (meters above ground level). A detailed depiction of the site location, trajectory clusters, and meteorological frequency distributions is illustrated in Fig. S1.

2.2 SP2 data analysis

In this study, the mass concentration and mixing state of BC were determined using a SP2. This instrument quantifies BC mass via the laser-induced incandescence (LII) technique. For clarity, the BC measured by the SP2 is hereafter referred to as refractory BC (rBC).

The operational principles of the SP2 have been described in detail elsewhere (Liu et al., 2010; Schwarz et al., 2006). Calibration of the incandescence signal was performed using Aquadag® black carbon particles (Aqueous Deflocculated Acheson Graphite, manufactured by Acheson Inc., USA), which yield a stronger incandescent response than ambient BC for the same mass. To correct for this difference, a correction factor of 0.75 was applied (Laborde et al., 2012). The mass-equivalent diameter of the rBC core (D_c) was calculated from the measured rBC mass, assuming a particle density of $1.8\,g\,cm^{-3}$ (Bond et al., 2013). Scattering signal calibration was conducted using polystyrene latex spheres (Nanosphere Size Standards, Duke Scientific Corp., Palo Alto, CA, USA) with diameters ranging from 50 to 600 nm. The distorted scattering signals generated by individual rBC particles were reconstructed using the leading-edge-only (LEO) fitting technique (Gao et al., 2007). The total particle diameter (D_p) was then derived by applying the measured D_c and reconstructed scattering signal to a core-shell Mie model, assuming a complex refractive index of $m = 2.26 + 1.26i$ for the rBC core (Moteki et al., 2010) and $m = 1.50 + 0i$ for the coating material (Laborde et al., 2012) at 1064 nm. Assuming the coating density of $1.5\,g\,cm^{-3}$ and the core density of $1.8\,g\,cm^{-3}$ (Cappa et al., 2012), the coating-to-core mass ratio (MR) was estimated over a defined time window using Eq. (1):

$$\mathrm{MR} = \frac{\rho_{\mathrm{coating}} \sum_{i=1}^{N} (D_{\mathrm{p,i}}^3 - D_{\mathrm{c,i}}^3)}{\rho_{\mathrm{core}} \sum_{i=1}^{N} D_{\mathrm{c,i}}^3} \quad (1)$$

where $D_{p,i}$ and $D_{c,i}$ represent the total particle diameter and the core diameter of an individual rBC particle, respectively. Notably, the MR presented here is not derived from direct measurements, but rather estimated based on SP2-derived parameters. As such, the estimated MR serves solely as an indicative proxy for assessing the mixing state of the bulk rBC population, rather than being used to calculate bulk optical properties.

To characterize the mass size distribution of rBC cores, the rBC mass detected by the SP2 was first allocated into discrete size bins spanning a diameter range of 70 to 500 nm. After calculating the mass concentration within each bin, the resulting size distribution was fitted with a lognormal function:

$$\frac{\mathrm{d}M}{\mathrm{d}\log D_c} = A \exp\left(-\frac{(\log D_c - \log D_0)^2}{2\log^2 \sigma_g}\right) \quad (2)$$

where A represents the peak mass concentration of the fitted distribution, D_0 denotes the mass median diameter (MMD), and σ_g is the geometric standard deviation (GSD) derived for each defined time window.

2.3 SPAMS data analysis

To investigate the chemical composition of BC-containing particles, a SPAMS was operated alongside the SP2 during the observation period. The operating principles of SPAMS have been described elsewhere (Li et al., 2011; Zhai et al., 2023). Over the entire sampling period, a total of 3 159 731 single-particle mass spectra were collected. Elemental carbon (EC) ion fragments were used as key markers of BC-containing particles (Spencer and Prather, 2006). Particles exhibiting EC ion signals with a relative peak area (RPA) greater than 0.1 were classified as BC-containing particles. Based on this threshold, 501 559 such particles were identified, accounting for approximately 15.9 % of the total particles detected by SPAMS. To further categorize the BC-containing particles, an adaptive resonance theory-based clustering algorithm (ART-2a) was employed (Song et al., 1999). This clustering analysis ultimately resulted in three distinct groups: EC, ECOC-NO_x, and ECOC-SO_x. The parameters used for ART-2a clustering were as follows: a learning rate of 0.8, a vigilance factor of 0.05, and 20 iterations.

The average mass spectral patterns of each particle type are shown in Fig. S2.

SPAMS exhibits optimal mass spectral detection efficiency for particles with aerodynamic diameters of 400–600 nm, the BC particles measured within this range are generally in an aged state. Temporal analysis shows that the number concentration of the EC cluster exhibits the strongest correlation with rBC number concentrations ($R^2 = 0.75$, Fig. S2). Given that EC particles typically preserve the initial chemical signatures of primary BC emissions, positive matrix factorization (PMF) analysis was applied to the relative peak areas (RPAs) of characteristic ion fragments within the EC cluster. By resolving the relative contributions of these characteristic chemical peaks, we aimed to trace the specific aging mechanisms of freshly emitted BC. Detailed procedures and parameter settings related to the PMF analysis are provided in the Supplement.

2.4 Particle optical property

A PAX (Droplet Measurement Technologies, USA) operating at a wavelength of 532 nm, was employed for in-situ measurements of aerosol optical properties. The scattering and absorption channels were calibrated using polystyrene latex (PSL) spheres and fullerene soot, respectively. The absorption coefficients measured by the PAX showed strong agreement with both the rBC mass concentrations derived from the SP2 ($R^2 = 0.95$) and the absorption coefficients calculated using a core-shell Mie model ($R^2 = 0.94$) (Fig. S4), indicating the reliability of the optical measurements. To quantify the absorption property of rBC, the mass absorption cross section (MAC) was calculated by combining the light absorption coefficient measured by the PAX with the rBC mass concentration derived from SP2, as follows:

$$\mathrm{MAC} = \frac{b_{\mathrm{abs}}}{[\mathrm{rBC}]} \tag{3}$$

where b_{abs} is the aerosol absorption coefficient measured by PAX and [rBC] is the rBC mass concentration from SP2.

Given that some BrC is known to absorb at 532 nm (Zhai et al., 2025) and measurements at longer wavelengths were unavailable, we adopted the method proposed by Cappa et al. (2019) to isolate the BrC contribution from the total absorption. First, the relative coating thickness of individual rBC particles was inferred based on the time lag between the peaks of the incandescence and scattering signals recorded by the SP2. Particles exhibiting a lag time greater than 2 μs were classified as thickly coated (Fig. S5a). Assuming that freshly emitted BC corresponds to a thinly coated population under ambient conditions, the intercept of the MAC obtained by extrapolating to a zero fraction of thickly coated particles was interpreted as the MAC of fresh BC (Lan et al., 2013), yielding a value of 7.13 $\mathrm{m^2\,g^{-1}}$, with a 95 % confidence interval of 6.57–7.78 $\mathrm{m^2\,g^{-1}}$ (Fig. S5b). The apparent absorption enhancement for each hourly interval was calculated as

$$E_{\mathrm{abs}} = \frac{\mathrm{MAC}}{\mathrm{MAC_{fresh}}}, \tag{4}$$

A campaign-specific relationship between E_{abs} and MR was subsequently established from the observations (Fig. 1a). This relationship was used to estimate the apparent absorption enhancement corresponding to the measured MR at each time interval. The BrC contribution was estimated as the residual between the measured total absorption and the estimated BC absorption:

$$b_{\mathrm{abs,BrC}} = b_{\mathrm{abs,obs}} - b_{\mathrm{abs,BC}} = b_{\mathrm{abs,obs}} - \mathrm{MAC_{BC,ref}} \cdot E_{\mathrm{abs}}(\mathrm{MR}) \cdot [\mathrm{rBC}] \tag{5}$$

where $b_{\mathrm{abs,BrC}}$, $b_{\mathrm{abs,obs}}$, and $b_{\mathrm{abs,BC}}$ are the absorption by BrC, the observed absorption, and the estimated absorption for BC particles, respectively. The resulting $b_{\mathrm{abs,BrC}}$ estimates were subsequently averaged by hour of day to obtain a mean diurnal profile (Fig. 1b). When calculating the MAC of rBC, the mean $b_{\mathrm{abs,BrC}}$ over the predefined daytime period was subtracted from the observed absorption during the corresponding daytime hours, after which the MAC was recalculated using the adjusted absorption coefficient. During daytime, the estimated BrC contribution accounted for 2 %–9 % of the measured absorption, corresponding to a MAC correction of 0.25–1.15 $\mathrm{m^2\,g^{-1}}$. In contrast, because high rBC concentrations dominate the optical absorption at night and yield physically meaningless negative $b_{\mathrm{abs,BrC}}$ values (Fig. 1b), the BrC contribution was not further corrected during nighttime. These negative values indicate that the nighttime BrC contribution could not be robustly resolved and was likely minor relative to BC absorption. This treatment does not imply the absence of nighttime BrC absorption, and the daytime correction should be regarded as a model-dependent adjustment. All optical and single-particle measurements were averaged to the same hourly time resolution before regression analysis and diurnal averaging.

3 Results and discussion

3.1 Overview of sampling period

Figure 2 illustrates temporal variations in measured meteorological parameters (temperature, humidity, and wind speed) together with concentrations of $PM_{2.5}$, O_3, NO_x, CO, and rBC from 21 November to 9 December 2021. Based on 72 h backward trajectory analyses, air masses were classified into three distinct clusters (Fig. S1a). Cluster 1 (C1), originating from the eastern coastal regions, dominanted from 21 November through 7–9 December. Cluster 3 (C3) represented long-range transport from the northwestern interior, influencing the site during 22–25 November and 1–3 December. Periods influenced by C3 were characterized by decreasing temperatures and relative humidity, typical signatures of wintertime cold waves, accompanied by stronger

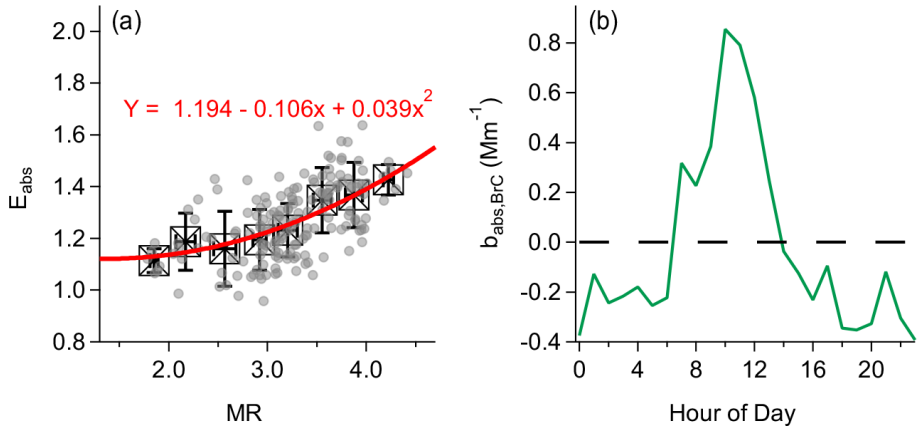

Figure 1. **(a)** Relationship between E_{abs} and MR at 532 nm. **(b)** Diurnal variation of brown carbon (BrC) absorption.

wind speeds and lower rBC concentrations (Figs. 2b and S1b). Despite the lower rBC levels, elevated MR during these intervals suggests an increased proportion of aged BC particles. In contrast, Cluster 2 (C2), which accounted for 41.23 % of the total sampling time, exhibited minimal spatial movement, thereby limiting the influence of long-range transport. Within the C2-dominated conditions, a continuous 7 d interval was identified (green box in Fig. 2) during which O_3, NO_x, CO and rBC all displayed consistent diurnal patterns. This period was therefore selected as a representative case dominated by the local emissions for detailed analysis of BC aging processes.

During this episode, ambient temperatures ranged from 11 to 26 °C (mean: 18 °C), and relative humidity varied between 26 % and 80 % (mean: 55 %) (Fig. 2a). The mean $PM_{2.5}$ concentration was 31.3 µg m^{-3}, indicating moderate pollution levels (Fig. 2b). The average rBC concentration was 1.2 µg m^{-3}, contributing approximately 3.8 % to the $PM_{2.5}$ mass. Furthermore, rBC showed strong correlations with NO_x ($R^2 = 0.71$, $p < 0.001$) and CO ($R^2 = 0.51$, $p < 0.001$), both recognized tracers of vehicular emissions in urban environments (Gong et al., 2016; Laborde et al., 2013; Liu et al., 2014). Besides, the sampling site is located in a densely trafficked urban area without major industrial sources nearby. The site characteristics and the observed pollutant correlations strongly suggest that local traffic emissions were the primary source of rBC during this period. Characterized by consistent diurnal variations in both meteorology and pollutants, relatively weak long-range transport, and traffic-dominated BC emissions, this episode provided a useful observational window for examining local diurnal BC aging processes. To evaluate the representativeness of the selected period, we further compared its diurnal variations with the full-campaign average (Figs. 3 and S6). The selected period showed generally consistent timing and direction of the key diurnal variations observed over the full campaign, whereas the full-period data exhibited greater variability, likely reflecting the influence of air masses associated with different trajectory clusters. These similarities suggest that the key diurnal patterns were not unique to the selected period, while the local-emissions subset provided a less heterogeneous observational context for examining daytime and nighttime BC evolution. While intense morning emissions were expected, the rBC concentration (Fig. 3c) exhibited a distinct bimodal pattern, with peaks occurring only during the evening rush hours (18:00–20:00 LT) and around midnight (00:00 LT). The absence of a morning peak is likely attributed to rapid dispersion associated with the rising mixing layer height (MLH) and wind speed (Fig. 3a, d). The midnight rBC peak coincided with significant increases in NO and CO concentrations (Fig. 3b, h). Given the lack of nearby industrial sources, this synchronized surge across NO and rBC likely points to emissions from heavy-duty diesel vehicles.

The size distribution of rBC cores further supports an urban traffic-dominated source. The MMD ranged from 155 to 170 nm (Fig. 3f) with relatively narrow and stable GSDs (1.55–1.58, Fig. S7), typical of urban vehicular sources (Li et al., 2023; Yang et al., 2022). A notable observation is the continuous increase of MMD in the nighttime from 155 to 170 nm. Normalized size distributions (Fig. S7b) indicate that the slight diurnal fluctuations in MMD were driven by the intermittent inputs of smaller, freshly emitted BC particles, rather than by regional transport. Given the minimal influence of external transport, variations in MR provide evidence for BC aging. The MR exhibited a continuous increase from 08:00 to 14:00 LT (Fig. 3i), correlated with O_x ($R^2 = 0.51$, Fig. S8), indicating that photochemical processing dominated daytime BC aging (Zhang et al., 2025). In addition, MR also increased during nighttime, suggesting nocturnal aging of BC. Similar behavior has been reported in previous studies under conditions conducive to heterogeneous reactions (Liu et al., 2022; Wei et al., 2023).

Distinct aging pathways during day and night are further corroborated by the diurnal distribution of rBC coating thickness (Fig. 4). During nighttime, BC particles exhibited grad-

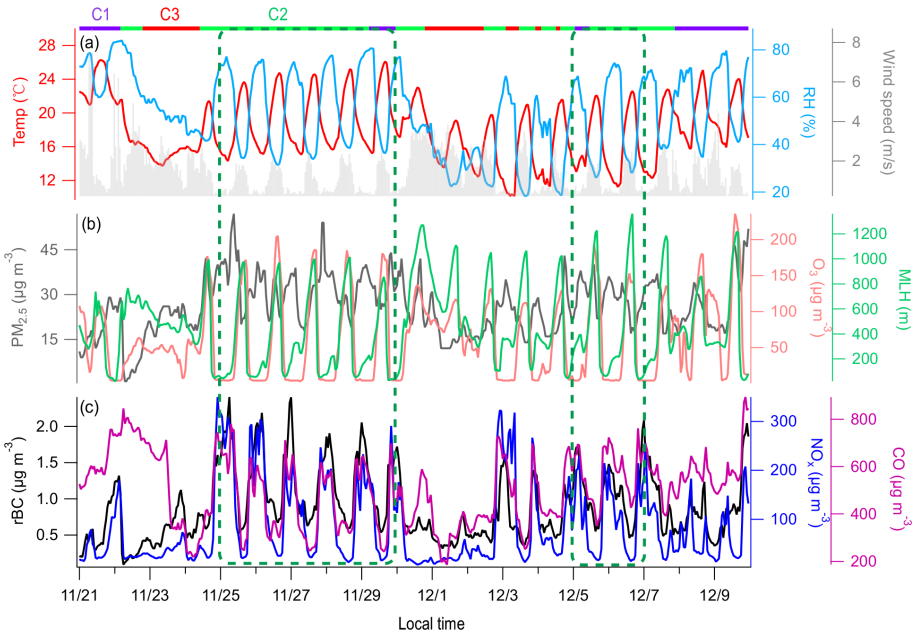

Figure 2. Temporal variations of meteorological parameters and pollutant mass concentrations with 60 min resolution. **(a)** Temperature, relative humidity (RH), and wind speed, **(b)** $PM_{2.5}$, O_3, and mixing layer height, **(c)** rBC and NO_x. The time period enclosed by the green box is defined as predominantly influenced by local emissions and the discussion focuses on these data.

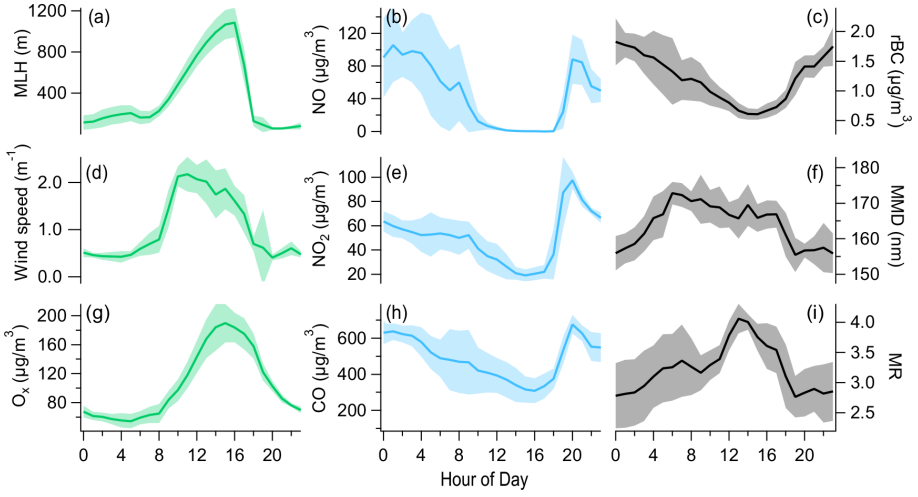

Figure 3. The diurnal variations of **(a)** MLH, **(b)** NO mass concentration, **(c)** rBC mass concentration, **(d)** wind speed, **(e)** NO_2 mass concentration, **(f)** MMD, **(g)** O_3 mass concentration, **(h)** CO mass concentration, and **(i)** MR. Data points denote hourly mean values, and the shaded areas represent ±1 standard deviation.

ual growth, with the coating thickness of the dominant population increasing by ∼ 10 nm. In contrast, daytime BC particles generally exhibited thinner coatings, primarily reflecting the continuous input of freshly emitted BC from intense daytime traffic emissions. Under active photochemical conditions, however, a secondary mode emerged at a coating thickness of ∼ 60 nm. The thinly coated mode was likely maintained by continuous local emissions near the surface, whereas the thickly coated secondary mode may have arisen from several concurrent processes, including rapid photochemical aging of a subset of BC particles and possible entrainment or downward mixing of more aged particles from aloft during planetary boundary layer (PBL) development. In addition, PBL expansion may preferentially disperse freshly emitted, thinly coated BC near the surface, thereby reducing its relative contribution to the normalized coating-thickness distribution. The observed daytime changes were consistent with the combined influence of boundary-layer entrainment

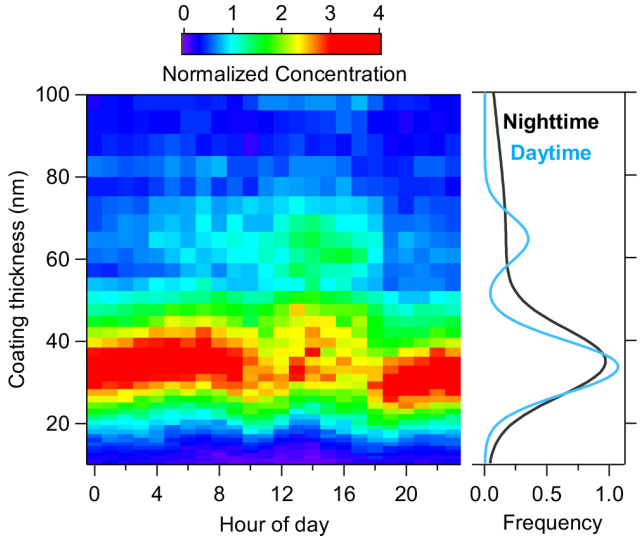

Figure 4. Diurnal variation in the coating thickness of rBC particles. The left panel presents a heatmap showing the distribution of coating thickness. The right panel shows normalized frequency distributions of coating thickness for nighttime (00:00–06:00 LT) and daytime (09:00–14:00 LT) periods, with overlaid lognormal fits to highlight differences. It should be noted that the diurnal variation of the coating thickness presented here is only for the rBC core with a diameter of 160 ± 20 nm, which was the dominant contributor to the total rBC mass concentration.

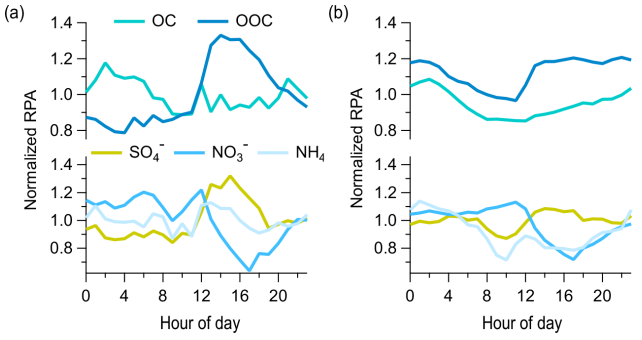

Figure 5. The normalized relative peak areas (RPA) of BC-containing particles **(a)** and non-BC particles **(b)** measured by SPAMS. OC is the sum of the representative organic species (m/z 27 [$C_2H_3^+$], 29 [$C_2H_5^+$], 51 [$C_4H_3^+$], -26 [CN^-]), OOC represents the sum of the oxygenated organic species (m/z 43 [CH_3CO^+], -57 [$C_2HO_2^-$], -89 [$C_2O_4H^-$]), SO_4^- represents m/z -97 [SO_4^-], NO_3^- represents m/z -62 [NO_3^-], and NH_4^+ represents m/z 18 [NH_4^+]. The RPA at each time point was normalized by dividing it by the average RPA over the entire sampling period.

and rapid photochemical aging, but the contribution of each process remains uncertain. The emergence of this bimodal distribution nevertheless highlights the pronounced heterogeneity of BC mixing state during daytime, in contrast to the more uniform coating characteristics observed at night.

3.2 Diurnal Aging Mechanisms of BC

The diurnal variations in the mixing state demonstrate that BC undergoes distinct daytime and nighttime aging processes. To further elucidate the chemical mechanisms driving these dynamic transformations, we examined the diurnal evolution of the chemical composition of BC-containing particles (Fig. 5). The diurnal variation of OC closely tracked that of the BC mass concentration (Fig. 3c). In contrast, oxygenated organic carbon (OOC) and sulfate (SO_4^{2-}) exhibited drastic increases during the daytime, indicative of secondary formation. Nitrate (NO_3^-) displayed a bimodal pattern, with one peak occurring at night and a second peak emerging during the early stages of daytime photochemistry. Ammonium (NH_4^+) increased concurrently during the day, aligning with the rising trends of both sulfate and nitrate. In comparison to non-BC particles (Fig. 5b), which share similar diurnal trends for other secondary species, BC-containing particles exhibit significantly greater RPA variability exclusively for SO_4^{2-}. The stronger sulfate signals observed in BC-containing particles are consistent with preferential sulfate accumulation on these particles, although the underlying mechanisms cannot be uniquely determined from the SPAMS measurements alone. BC-involved photochemistry has been proposed as one possible mechanism for enhanced sulfate accumulation in previous studies (Guo et al., 2025; Zhang et al., 2021), but its contribution to the present observations requires further investigation.

Coagulation may also contribute to the diurnal evolution of the BC mixing state by transferring pre-existing secondary material from non-BC particles to the BC-containing population. This process may be more favorable under higher particle number concentrations and weaker atmospheric dispersion, conditions that occurred more frequently during nighttime in this study (Fig. 3c). The observed nighttime increase in MMD (Fig. 3f) is consistent with particle growth but cannot be uniquely attributed to coagulation, because condensation, heterogeneous uptake, and changes in particle sources may also contribute. During daytime, PBL development and stronger atmospheric dispersion may reduce particle concentrations and thereby decrease the likelihood of coagulation. Nevertheless, quantitative coagulation timescales cannot be constrained with the available measurements. Therefore, the observed increases in rBC coating thickness and secondary species associated with BC-containing particles cannot be unambiguously attributed to direct condensation or heterogeneous uptake, as coagulation-driven mixing may also contribute.

To further resolve the aging processes of freshly emitted BC, PMF analysis was applied to particles within the EC cluster. This approach decomposes complex mass spectral data into distinct chemical factors and their temporal contributions (Zauscher et al., 2013). The resulting factor profiles and diurnal patterns are shown in Fig. 6. A sub-

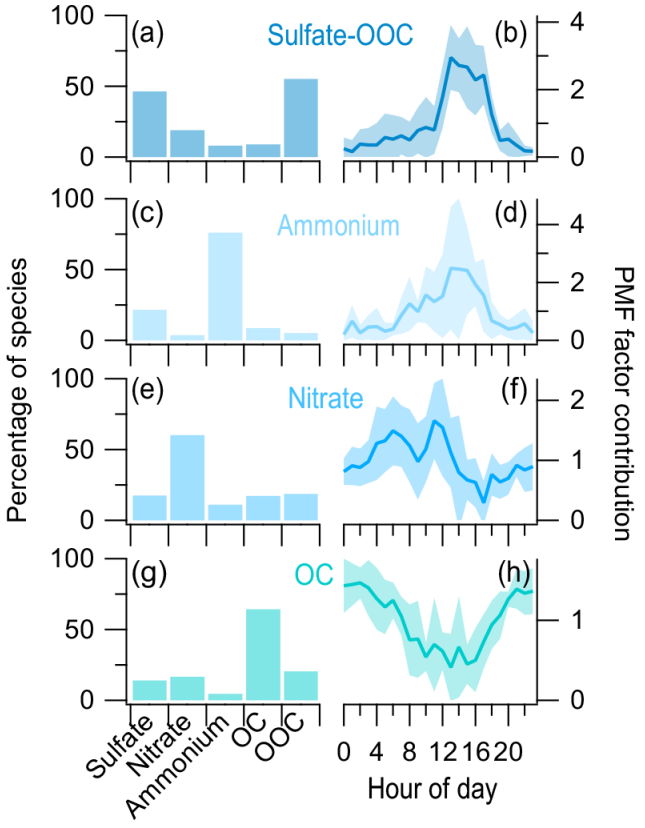

Figure 6. **(a, c, e, g)** PMF-resolved four source profiles and **(b, d, f, h)** their diurnal profile of contributions.

stantial increase in the Nitrate factor was observed during nighttime, indicating enhanced nitrate accumulation on BC-containing particles. Several processes may have contributed to this nighttime enhancement. The elevated nighttime NO_2 levels (Fig. 3e), together with the presence of O_3 (Fig. 3g), may provide conditions favorable for NO_3/N_2O_5 chemistry, and heterogeneous hydrolysis of N_2O_5 on particle surfaces could therefore contribute to nitrate formation. However, this pathway cannot be directly constrained in the absence of NO_3 and N_2O_5 measurements. Thermodynamic gas–particle partitioning may also contribute to the observed nitrate enhancement. In particular, lower nighttime temperatures and higher RH may favor the partitioning of semi-volatile nitrate into the particle phase, while the presence of sufficient NH_3 and aerosol liquid water could further promote particulate NH_4NO_3 formation (Guo et al., 2016, 2017). Therefore, the observed nighttime nitrate accumulation likely reflects the combined influence of heterogeneous nitrogen chemistry and thermodynamic partitioning, although their relative contributions cannot be quantified with the available measurements.

During the early stage of daytime photochemical aging, the contribution of the nitrate factor began increasing earlier than that of the Sulfate–OOC factor. This temporal offset may be explained by two possible mechanisms: (1) SO_4^{2-} precursors may not have reached sufficient concentrations at that time (Zhang et al., 2021; Zhou et al., 2022); and (2) gaseous HNO_3 formed via photochemical reactions may have been directly taken up by BC particles through heterogeneous processes (Choi and Leu, 1998; Prince et al., 2002). However, the available observations do not permit a definitive determination of the dominant pathway. The Sulfate–OOC factor reached its maximum between 11:00 and 14:00 LT, coinciding with a pronounced increase in the ammonium factor. This concurrence suggests enhanced formation of $(NH_4)_2SO_4$ and other secondary photochemical products, leading to accelerated BC aging through condensational growth.

In alignment with the bulk BC-containing particle population, the primary EC cluster exhibits similar trends in secondary species accumulation. This consistency across different analytical approaches explicitly highlights the highly dynamic nature of BC aging, pointing to distinct chemical evolutionary pathways operating under daytime and nighttime atmospheric conditions.

3.3 Diurnal Variations of BC optical properties

The diurnal aging of BC observed during the sampling period was accompanied by corresponding changes in its optical properties. As shown in Fig. 7a, the MAC reached a minimum of approximately 8.1 $m^2\ g^{-1}$ at 22:00 LT. Thereafter, it increased by approximately 0.8 $m^2\ g^{-1}$ overnight, reaching 8.9 $m^2\ g^{-1}$ by 06:00 LT. A comparable enhancement occurred during the daytime photochemically active period, when MAC increased by approximately 1.0 $m^2\ g^{-1}$, from 8.9 to 9.9 $m^2\ g^{-1}$. The observed MAC range of 8.1–9.9 $m^2\ g^{-1}$ falls within the range previously reported for urban BC. At wavelength of 532 nm, Lan et al. (2013) reported MAC values of 5.0–8.5 $m^2\ g^{-1}$ in summertime Shenzhen. A higher campaign-average MAC of $14.6 \pm 5.6\ m^2\ g^{-1}$ was reported for urban Xi'an using an SP2–PAX system (Wang et al., 2017). In urban Beijing, Liu et al. (2019) further showed that the modeled MAC at 550 nm varied substantially with BC mixing state, ranging from approximately 5.3–7.3 $m^2\ g^{-1}$ for largely uncoated or thinly coated BC to 11.2–12.4 $m^2\ g^{-1}$ for moderately or thickly coated BC.

Although the daytime increase occurred over a shorter period than the nighttime increase, the comparable net enhancements in MAC during both periods indicate that multiple atmospheric processes jointly influenced the evolution of BC optical properties. BC particles in the early stages of aging exhibit negligible light absorption enhancement, however, as aging proceeds and a core–shell morphology develops, coating-induced lensing can substantially enhance their light absorption (Peng et al., 2016; Liu et al., 2017; Wu et al., 2018). Following Liu et al. (2017), $MR > 3$ was used as a qualitative indicator to identify highly coated BC-containing particles whose optical behavior is consistent with a core–shell morphology. The mass fraction of rBC associated with

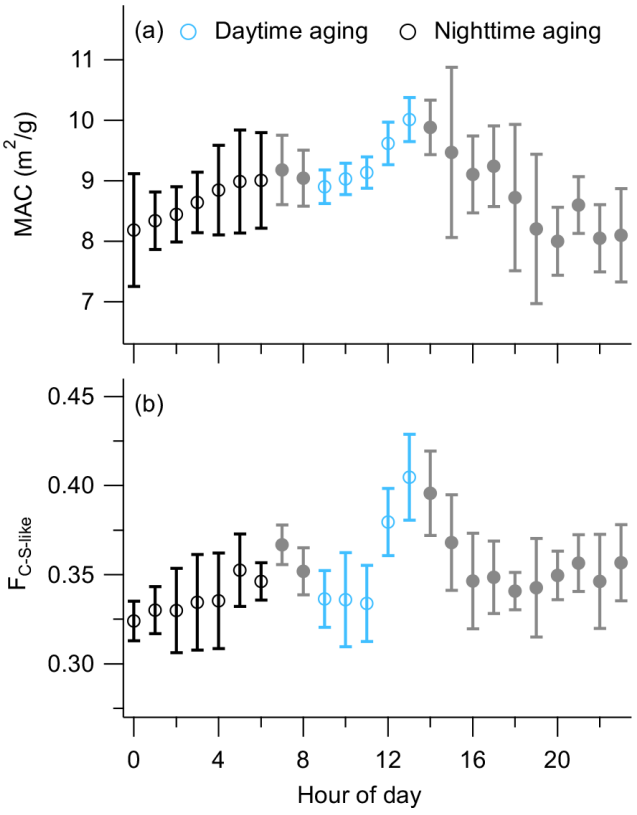

Figure 7. **(a)** Diurnal variation in the MAC of rBC at 532 nm. **(b)** The mass fraction of core-shell-like rBC exhibiting absorption enhancement.

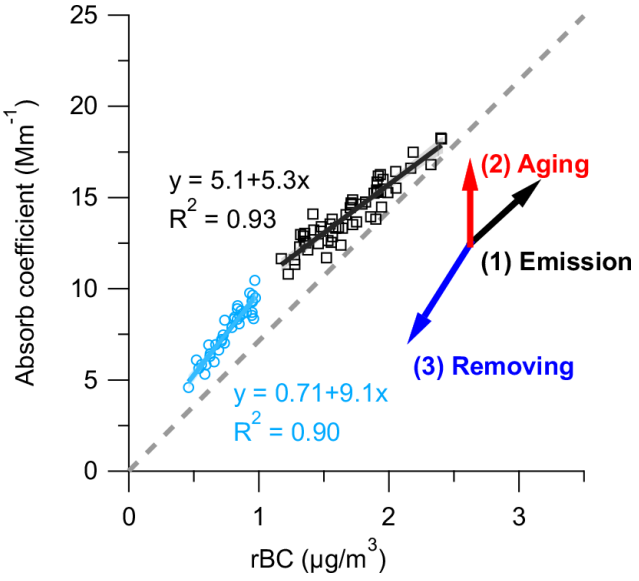

Figure 8. Scatter plot of the light absorption coefficient and rBC mass concentration, with data points colored by daytime (blue) and nighttime (black) periods. The gray dashed line indicates the expected relationship assuming all rBC particles are freshly emitted. Red arrows denote the directional shifts in the scatter plot induced by (1) fresh emissions, (2) atmospheric aging, and (3) removal processes.

these particles was calculated as:

$$F_{\text{C-S-like}} = \frac{\sum_{i:\,\text{MR}_i>3} m_{\text{rBC},i}}{\sum_i m_{\text{rBC},i}}, \quad (6)$$

where $m_{\text{rBC},i}$ denotes the rBC mass of the ith particle, and $F_{\text{C-S-like}}$ represents the fraction of total rBC mass associated with particles classified as core–shell-like. The MR threshold here was used only for particle classification, while F_{thickly} represents the quantitatively calculated fraction of total rBC mass carried by particles within this highly coated regime. As Fig. 7b shows, the $F_{\text{C-S-like}}$ increased from 0.32 to 0.35 during the night, decreased to 0.32 following the morning rush hour, and subsequently rose to 0.40 after daytime photochemical aging. Notably, the magnitude of this diurnal change is substantially larger than the observed day-night variation in bulk MAC.

In the ambient atmosphere, the bulk optical properties of BC are influenced not only by aging but also by emissions, regional transport, and atmospheric removal processes. Given the minimal influence of transport during the selected period, the observed diurnal variation of the MAC is governed by the interplay of fresh emissions, aging, and atmospheric removal. These competing effects can be visualized in the two-dimensional relationship between the bulk absorption coefficient and rBC mass (Fig. 8). The fresh-emission trajectory (black arrow), in which absorption and rBC mass increase proportionally, was defined using an empirical fresh-BC-equivalent MAC baseline ($\text{MAC}_{\text{fresh}}$). This baseline was obtained by extrapolating the empirical relationship between MAC and the fraction of thickly coated BC particles to a zero thickly coated fraction. The resulting $\text{MAC}_{\text{fresh}}$ was 7.13 $\text{m}^2\,\text{g}^{-1}$, with a 95 % confidence interval of 6.57–7.78 $\text{m}^2\,\text{g}^{-1}$. This value is comparable in magnitude to previously reported MAC values for fresh or uncoated BC, including $6.5 \pm 0.5\ \text{m}^2\,\text{g}^{-1}$ at 532 nm in urban Shenzhen (Lan et al., 2013), $7.5 \pm 1.2\ \text{m}^2\,\text{g}^{-1}$ at 550 nm for uncoated carbonaceous particles (Bond and Bergstrom, 2006), and $8.0 \pm 0.7\ \text{m}^2\,\text{g}^{-1}$ at 550 nm for freshly emitted BC (Asmi et al., 2025). Although these values were obtained under different measurement conditions and definitions of fresh BC, their comparable magnitudes provide useful context for the empirical baseline derived here. Aging enhances absorption without adding rBC mass, resulting in a vertical shift (red arrow). In contrast, removal processes reduce rBC mass and preferentially remove aged particles, yielding a trajectory with a slope larger than $\text{MAC}_{\text{fresh}}$ (blue arrow).

To isolate absorption changes attributable to the optical variations driven solely by atmospheric aging, linear regressions were applied to the data collected during the respective daytime and nighttime aging periods. This approach estimates the deviation of the measured absorption coefficient from the theoretical baseline, assuming fresh emissions at the

same rBC mass concentration. The difference represents the additional absorption coefficient induced by the lensing effect ($b_{E_{abs}}$), which can be quantified as follows:

$$b_{E_{abs}} = b_{abs,obs} - MAC_{fresh} \cdot [rBC] \quad (7)$$

where MAC_{fresh} represents the MAC of freshly emitted rBC and [rBC] denotes the rBC core mass concentration. Although the potential interference from fresh emissions cannot be entirely isolated, $b_{E_{abs}}$ serves as a useful proxy for characterizing the optical variations driven by daytime and nighttime aging. As $b_{E_{abs}}$ is dominated by contributions from thickly coated BC particles, we quantified the MAC of thickly coated BC and the temporal rates of MAC change driven by atmospheric aging:

$$MAC_{C\text{-}S\text{-}like} = \frac{b_{E_{abs}} + MAC_{fresh} \cdot [rBC] \cdot F_{C\text{-}S\text{-}like}}{[rBC] \cdot F_{C\text{-}S\text{-}like}} \quad (8)$$

$$R_{MAC,C\text{-}S\text{-}like} = \frac{MAC_{C\text{-}S\text{-}like,\,max} - MAC_{C\text{-}S\text{-}like,\,min}}{\Delta t} \quad (9)$$

where $F_{C\text{-}S\text{-}like}$ denotes the fraction of total rBC mass associated with particles classified as core–shell-like, Δt represents the elapsed time between the occurrences of the minimum and maximum $MAC_{C\text{-}S\text{-}like}$ values within the respective daytime and nighttime periods, and $R_{MAC,C\text{-}S\text{-}like}$ denotes the corresponding apparent MAC enhancement rate. The coating thickness and MR derived from the SP2 LEO-fit analysis should be regarded as model-dependent estimates rather than directly measured quantities. The retrieved coating thickness is sensitive to assumptions regarding the refractive indices of the rBC core and coating, while the calculated MR additionally depends on the assumed core and coating densities. Deviations from the idealized concentric core–shell morphology may introduce further uncertainty. Consequently, these assumptions may affect the absolute values of the retrieved coating thickness, MR, and the classification of particles close to the operational MR = 3 threshold. These uncertainties should therefore be considered when interpreting the quantitatively derived coating properties. The parameter sensitivity was further evaluated by varying the MR threshold, coating density, and MAC_{fresh}. For each parameter combination, $MAC_{C\text{-}S\text{-}like}$ and $F_{C\text{-}S\text{-}like}$ were recalculated, and the daytime and nighttime rates were derived. As shown in Fig. 9, the derived rates varied with the MR threshold, coating density, and MAC_{fresh}. The nearly vertical contours in the daytime panels indicate a stronger sensitivity to MAC_{fresh}, reflecting the larger daytime variation in $F_{C\text{-}S\text{-}like}$. In contrast, the nighttime rates were more sensitive to coating density, likely because density-induced changes in MR resulted in stronger reclassification of particles near the prescribed threshold. The sensitivity results are summarized in the boxplots (Fig. 9d and h), with the daytime and nighttime $R_{MAC,C\text{-}S\text{-}like}$ of 0.51 ± 0.11 and $0.36 \pm 0.05\ m^2\ g^{-1}\ h^{-1}$, respectively.

It should be emphasized that these rates are campaign-specific estimates derived from the temporal changes in MAC observed during this campaign and evaluated over the empirical parameter ranges considered in the sensitivity analysis. Several instrumental limitations introduce additional uncertainty. Residual BrC absorption at 532 nm may affect the absorption attributed to BC. The SP2 cannot directly resolve the actual morphology of ambient BC particles; therefore, the MR-based identification of core-shell-like BC should be regarded as an optically equivalent classification. Nevertheless, previous urban observations provide useful context for the optical evolution identified here. Wang et al. (2017) reported an increase in bulk rBC MAC of $0.60\ m^2\ g^{-1}\ h^{-1}$ during a daytime photochemical period in urban Xi'an. Peng et al. (2016) found that the BC absorption enhancement factor reached approximately 2.4 after about 5 h in Beijing and 18 h in Houston. In urban Guangzhou, Sun et al. (2020) observed enhanced E_{abs} during the afternoon in the dry season and elevated nighttime E_{abs} during the wet season. Although these studies used different optical metrics, their results demonstrate that substantial BC optical evolution can occur over timescales of several hours in urban environments. BC optical properties evolve nonlinearly as particle morphology and composition change during atmospheric aging (Wang et al., 2021b). These observations may also provide useful constraints for evaluating model representations of BC aging and optical evolution. Recent modeling studies have incorporated observation-constrained BC mixing-state and optical properties to improve estimates of BC radiative effects (Chen et al., 2023). In this context, the observed diurnal evolution of BC coating state and MAC can provide benchmarks for evaluating whether models reproduce the characteristic timescales and magnitude of BC optical changes under urban atmospheric conditions. In particular, the contrasting daytime and nighttime evolution highlights the potential importance of representing temporally varying aging environments rather than assuming a single constant aging timescale. The observed relationship between BC coating state and optical enhancement may also help evaluate parameterizations linking BC mixing state to MAC.

4 Conclusions

This study provides a comprehensive characterization of BC in urban Shenzhen during a sampling period with minimal regional transport influence and dominant local vehicular emissions.

The average rBC mass concentration was $1.2\ \mu g\ m^{-3}$, with strong correlations to NO_x and CO. The MMD of rBC cores ranged from 155 to 170 nm. By integrating coating information derived from SP2 with chemical composition data from SPAMS and PMF analysis, we elucidated distinct diurnal aging mechanisms of BC under real-world conditions. Nighttime aging was characterized by increased nitrate signals and coating thickness. These changes may reflect the combined effects of gas–particle partitioning, condensation

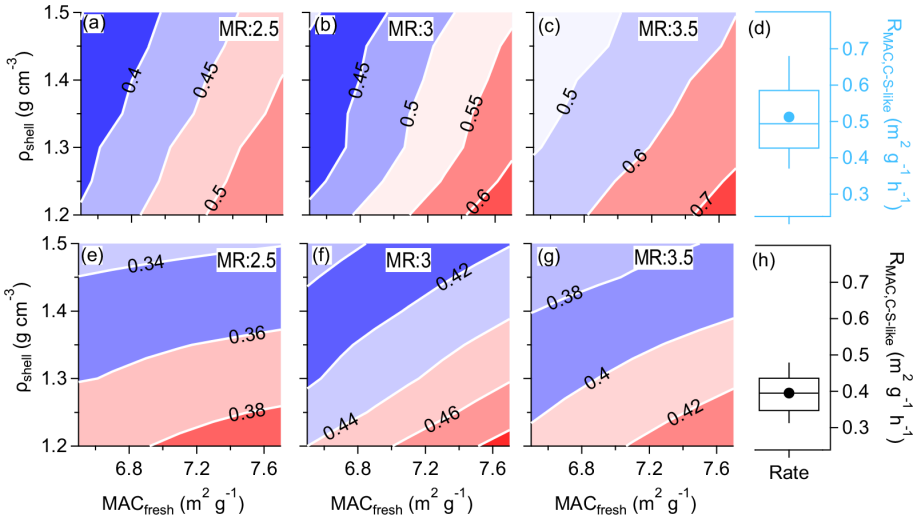

Figure 9. Sensitivity of the apparent MAC enhancement rate ($R_{\mathrm{MAC,C\text{-}S\text{-}like}}$) to $\mathrm{MAC_{fresh}}$, coating density (ρ_{coating}), and the MR threshold. The upper **(a–c)** and lower **(e–g)** panels represent daytime and nighttime rates, respectively. The three columns correspond to MR thresholds of 2.5, 3.0, and 3.5. Shading and contours indicate $R_{\mathrm{MAC,C\text{-}S\text{-}like}}$ ($\mathrm{m^2\,g^{-1}\,h^{-1}}$). **(d)** and **(h)** summarize the distributions of the daytime and nighttime $R_{\mathrm{MAC,C\text{-}S\text{-}like}}$ obtained across all sensitivity scenarios, respectively.

of secondary species, and coagulation. Daytime photochemical aging was characterized by rapid ammonium nitrate accumulation, followed by delayed increases in sulfate and oxidized organic species. The sulfate variations were consistent with preferential sulfate accumulation on BC-containing particles. Together, these processes produced bimodal diurnal variations in coating thickness and secondary species accumulation.

The evolving mixing state exerted profound influences on BC optical properties, with the MAC at 532 nm increasing by $\sim 0.8\,\mathrm{m^2\,g^{-1}}$ overnight and $\sim 1.0\,\mathrm{m^2\,g^{-1}}$ during the daytime. By classifying BC particles according to the MR threshold, we tracked the MAC evolution of core–shell-like BC during the nighttime and daytime periods. The corresponding $R_{\mathrm{MAC,C\text{-}S\text{-}like}}$ were 0.36 ± 0.05 and $0.51 \pm 0.11\,\mathrm{m^2\,g^{-1}\,h^{-1}}$, respectively. The mean daytime rate was approximately 1.4 times the nighttime rate, indicating faster optical evolution during the daytime period. These values represent campaign-specific apparent rates for core–shell-like BC during the selected urban episode. Although photochemical aging proceeds significantly faster, the comparable magnitudes of the total nocturnal and diurnal MAC increments indicate that the rapid daytime coating accumulation was partially offset by the dilution and removal of aged particles during mixing layer expansion.

Data availability. Data used to produce the plots within this work are available in Zenodo (https://doi.org/10.5281/zenodo.21973372, Zhang, 2026).

Supplement. The supplement related to this article is available online at https://doi.org/10.5194/acp-26-12197-2026-supplement.

Author contributions. YZ, JZ and XY designed the study. YZ and JZ analyzed the data. YZ wrote the manuscript. All co-authors contributed to discussions and suggestions in finalizing the manuscript.

Competing interests. The contact author has declared that none of the authors has any competing interests.

Disclaimer. Publisher's note: Copernicus Publications remains neutral with regard to jurisdictional claims made in the text, published maps, institutional affiliations, or any other geographical representation in this paper. The authors bear the ultimate responsibility for providing appropriate place names. Views expressed in the text are those of the authors and do not necessarily reflect the views of the publisher.

Acknowledgements. This work was supported by the National Natural Science Foundation of China (grant no. 42530609), the Guangdong Provincial Field Observation and Research Station for Coastal Atmosphere and Climate of the Greater Bay Area, Southern University of Science and Technology, Shenzhen, Guangdong, China (grant no. 518055), the Guangdong Provincial Field Observation and Research Station for Coastal Atmosphere and Climate of the Greater Bay Area (grant no. 2021B1212050024), the Shenzhen Science and Technology Program (grant nos. KQTD20210811090048025, KCXFZ20230731093601003), the Ministry of Science and Technology of the People's Republic of

China (grant no. 2023YFE0112901), and the High level of special funds (grant no. G03050K001).

Financial support. This research has been supported by the National Natural Science Foundation of China (grant no. 42530609), the Guangdong Provincial Field Observation and Research Station for Coastal Atmosphere and Climate of the Greater Bay Area, Southern University of Science and Technology, Shenzhen, Guangdong, China (grant no. 518055), the Guangdong Provincial Field Observation and Research Station for Coastal Atmosphere and Climate of the Greater Bay Area (grant no. 2021B1212050024), the Shenzhen Science and Technology Program (grant nos. KQTD20210811090048025, KCXFZ20230731093601003), the Ministry of Science and Technology of the People's Republic of China (grant no. 2023YFE0112901), and the High level of special funds (grant no. G03050K001).

Review statement. This paper was edited by Theodora Nah and reviewed by two anonymous referees.

References

Asmi, E., Sipkens, T. A., Saturno, J., Backman, J., Vasilatou, K., Weingartner, E., Keller, A., Ciupek, K., Müller, T., Babu Suja, A., Močnik, G., Drinovec, L., Eleftheriadis, K., Gini, M. I., Nowak, A., and Corbin, J. C.: Mass absorption cross-section of ambient black carbon aerosols - a review, npj Climate and Atmospheric Science, 9, 17, https://doi.org/10.1038/s41612-025-01288-2, 2025.

Baumgartner, J., Zhang, Y., Schauer, J. J., Huang, W., Wang, Y., and Ezzati, M.: Highway proximity and black carbon from cookstoves as a risk factor for higher blood pressure in rural China, P. Natl. Acad. Sci. USA, 111, 13229–13234, https://doi.org/10.1073/pnas.1317176111, 2014.

Bond, T. C. and Bergstrom, R. W.: Light Absorption by Carbonaceous Particles: An Investigative Review, Aerosol Sci. Technol., 40, 27–67, https://doi.org/10.1080/02786820500421521, 2006.

Bond, T. C., Doherty, S. J., Fahey, D. W., Forster, P. M., Berntsen, T., DeAngelo, B. J., Flanner, M. G., Ghan, S., Kärcher, B., Koch, D., Kinne, S., Kondo, Y., Quinn, P. K., Sarofim, M. C., Schultz, M. G., Schulz, M., Venkataraman, C., Zhang, H., Zhang, S., Bellouin, N., Guttikunda, S. K., Hopke, P. K., Jacobson, M. Z., Kaiser, J. W., Klimont, Z., Lohmann, U., Schwarz, J. P., Shindell, D., Storelvmo, T., Warren, S. G., and Zender, C. S.: Bounding the role of black carbon in the climate system: A scientific assessment, J. Geophys. Res.-Atmos., 118, 5380–5552, https://doi.org/10.1002/jgrd.50171, 2013.

Cappa, C. D., Onasch, T. B., Massoli, P., Worsnop, D. R., Bates, T. S., Cross, E. S., Davidovits, P., Hakala, J., Hayden, K. L., Jobson, B. T., Kolesar, K. R., Lack, D. A., Lerner, B. M., Li, S.-M., Mellon, D., Nuaaman, I., Olfert, J. S., Petäjä, T., Quinn, P. K., Song, C., Subramanian, R., Williams, E. J., and Zaveri, R. A.: Radiative Absorption Enhancements Due to the Mixing State of Atmospheric Black Carbon, Science, 337, 1078–1081, https://doi.org/10.1126/science.1223447, 2012.

Cappa, C. D., Zhang, X., Russell, L. M., Collier, S., Lee, A. K. Y., Chen, C., Betha, R., Chen, S., Liu, J., Price, D. J., Sanchez, K. J., McMeeking, G. R., Williams, L. R., Onasch, T. B., Worsnop, D. R., Abbatt, J., and Zhang, Q.: Light Absorption by Ambient Black and Brown Carbon and its Dependence on Black Carbon Coating State for Two California, USA, Cities in Winter and Summer, J. Geophys. Res.-Atmos., 124, 1550–1577, https://doi.org/10.1029/2018JD029501, 2019.

Chen, G., Wang, J., Wang, Y., Wang, J., Jin, Y., Cheng, Y., Yin, Y., Liao, H., Ding, A., Wang, S., Hao, J., and Liu, C.: An Aerosol Optical Module With Observation-Constrained Black Carbon Properties for Global Climate Models, J. Adv. Model. Earth Sy., 15, e2022MS003501, https://doi.org/10.1029/2022MS003501, 2023.

Choi, W. and Leu, M.-T.: Nitric Acid Uptake and Decomposition on Black Carbon (Soot) Surfaces: Its Implications for the Upper Troposphere and Lower Stratosphere, J. Phys. Chem. A, 102, 7618–7630, https://doi.org/10.1021/jp981647x, 1998.

Fierce, L., Bond, T. C., Bauer, S. E., Mena, F., and Riemer, N.: Black carbon absorption at the global scale is affected by particle-scale diversity in composition, Nat Commun., 7, 12361, https://doi.org/10.1038/ncomms12361, 2016.

Fuller, K. A., Malm, W. C., and Kreidenweis, S. M.: Effects of mixing on extinction by carbonaceous particles, J. Geophys. Res.-Atmos., 104, 15941–15954, https://doi.org/10.1029/1998JD100069, 1999.

Gao, R. S., Schwarz, J. P., Kelly, K. K., Fahey, D. W., Watts, L. A., Thompson, T. L., Spackman, J. R., Slowik, J. G., Cross, E. S., Han, J.-H., Davidovits, P., Onasch, T. B., and Worsnop, D. R.: A Novel Method for Estimating Light-Scattering Properties of Soot Aerosols Using a Modified Single-Particle Soot Photometer, Aerosol Sci. Technol., 41, 125–135, https://doi.org/10.1080/02786820601118398, 2007.

Gong, X., Zhang, C., Chen, H., Nizkorodov, S. A., Chen, J., and Yang, X.: Size distribution and mixing state of black carbon particles during a heavy air pollution episode in Shanghai, Atmos. Chem. Phys., 16, 5399–5411, https://doi.org/10.5194/acp-16-5399-2016, 2016.

Guo, H., Sullivan, A. P., Campuzano-Jost, P., Schroder, J. C., Lopez-Hilfiker, F. D., Dibb, J. E., Jimenez, J. L., Thornton, J. A., Brown, S. S., Nenes, A., and Weber, R. J.: Fine particle pH and the partitioning of nitric acid during winter in the northeastern United States, J. Geophys. Res.-Atmos., 121, 10355–10376, https://doi.org/10.1002/2016JD025311, 2016.

Guo, H., Liu, J., Froyd, K. D., Roberts, J. M., Veres, P. R., Hayes, P. L., Jimenez, J. L., Nenes, A., and Weber, R. J.: Fine particle pH and gas–particle phase partitioning of inorganic species in Pasadena, California, during the 2010 CalNex campaign, Atmos. Chem. Phys., 17, 5703–5719, https://doi.org/10.5194/acp-17-5703-2017, 2017.

Guo, Z., Qiu, P., Song, H., Ye, C., Du, Y., and Lu, K.: Insights into black carbon-activated manganese catalysis in atmospheric sulfate production, Sci. Bull., 70, 3659–3666, https://doi.org/10.1016/j.scib.2025.09.041, 2025.

Jacobson, M. Z.: Strong radiative heating due to the mixing state of black carbon in atmospheric aerosols, Nature, 409, 695–697, https://doi.org/10.1038/35055518, 2001.

Laborde, M., Schnaiter, M., Linke, C., Saathoff, H., Naumann, K.-H., Möhler, O., Berlenz, S., Wagner, U., Taylor, J. W., Liu, D.,

Flynn, M., Allan, J. D., Coe, H., Heimerl, K., Dahlkötter, F., Weinzierl, B., Wollny, A. G., Zanatta, M., Cozic, J., Laj, P., Hitzenberger, R., Schwarz, J. P., and Gysel, M.: Single Particle Soot Photometer intercomparison at the AIDA chamber, Atmos. Meas. Tech., 5, 3077–3097, https://doi.org/10.5194/amt-5-3077-2012, 2012.

Laborde, M., Crippa, M., Tritscher, T., Jurányi, Z., Decarlo, P. F., Temime-Roussel, B., Marchand, N., Eckhardt, S., Stohl, A., Baltensperger, U., Prévôt, A. S. H., Weingartner, E., and Gysel, M.: Black carbon physical properties and mixing state in the European megacity Paris, Atmos. Chem. Phys., 13, 5831–5856, https://doi.org/10.5194/acp-13-5831-2013, 2013.

Lan, Z.-J., Huang, X.-F., Yu, K.-Y., Sun, T.-L., Zeng, L.-W., and Hu, M.: Light absorption of black carbon aerosol and its enhancement by mixing state in an urban atmosphere in South China, Atmos. Environ., 69, 118–123, https://doi.org/10.1016/j.atmosenv.2012.12.009, 2013.

Li, F., Luo, B., Zhai, M., Liu, L., Zhao, G., Xu, H., Deng, T., Deng, X., Tan, H., Kuang, Y., and Zhao, J.: Black carbon content of traffic emissions significantly impacts black carbon mass size distributions and mixing states, Atmos. Chem. Phys., 23, 6545–6558, https://doi.org/10.5194/acp-23-6545-2023, 2023.

Li, L., Huang, Z., Dong, J., Li, M., Gao, W., Nian, H., Fu, Z., Zhang, G., Bi, X., Cheng, P., and Zhou, Z.: Real time bipolar time-of-flight mass spectrometer for analyzing single aerosol particles, Int. J. Mass Spectrom., 303, 118–124, https://doi.org/10.1016/j.ijms.2011.01.017, 2011.

Li, M., Bao, F., Zhang, Y., Sheng, H., Chen, C., and Zhao, J.: Photochemical Aging of Soot in the Aqueous Phase: Release of Dissolved Black Carbon and the Formation of $^1O_2$, Environ. Sci. Technol., 53, 12311–12319, https://doi.org/10.1021/acs.est.9b02773, 2019.

Liu, D., Flynn, M., Gysel, M., Targino, A., Crawford, I., Bower, K., Choularton, T., Jurányi, Z., Steinbacher, M., Hüglin, C., Curtius, J., Kampus, M., Petzold, A., Weingartner, E., Baltensperger, U., and Coe, H.: Single particle characterization of black carbon aerosols at a tropospheric alpine site in Switzerland, Atmos. Chem. Phys., 10, 7389–7407, https://doi.org/10.5194/acp-10-7389-2010, 2010.

Liu, D., Allan, J. D., Young, D. E., Coe, H., Beddows, D., Fleming, Z. L., Flynn, M. J., Gallagher, M. W., Harrison, R. M., Lee, J., Prevot, A. S. H., Taylor, J. W., Yin, J., Williams, P. I., and Zotter, P.: Size distribution, mixing state and source apportionment of black carbon aerosol in London during wintertime, Atmos. Chem. Phys., 14, 10061–10084, https://doi.org/10.5194/acp-14-10061-2014, 2014.

Liu, D., Whitehead, J., Alfarra, M. R., Reyes-Villegas, E., Spracklen, D. V., Reddington, C. L., Kong, S., Williams, P. I., Ting, Y.-C., Haslett, S., Taylor, J. W., Flynn, M. J., Morgan, W. T., McFiggans, G., Coe, H., and Allan, J. D.: Black-carbon absorption enhancement in the atmosphere determined by particle mixing state, Nat. Geosci., 10, 184–188, https://doi.org/10.1038/ngeo2901, 2017.

Liu, D., Joshi, R., Wang, J., Yu, C., Allan, J. D., Coe, H., Flynn, M. J., Xie, C., Lee, J., Squires, F., Kotthaus, S., Grimmond, S., Ge, X., Sun, Y., and Fu, P.: Contrasting physical properties of black carbon in urban Beijing between winter and summer, Atmos. Chem. Phys., 19, 6749–6769, https://doi.org/10.5194/acp-19-6749-2019, 2019.

Liu, H., Pan, X., Wang, D., Liu, X., Tian, Y., Yao, W., Lei, S., Zhang, Y., Li, J., Lei, L., Xie, C., Fu, P., Sun, Y., and Wang, Z.: Mixing characteristics of black carbon aerosols in a coastal city using the CPMA-SP2 system, Atmos. Res., 265, 105867, https://doi.org/10.1016/j.atmosres.2021.105867, 2022.

Moteki, N., Kondo, Y., and ichi Nakamura, S.: Method to measure refractive indices of small nonspherical particles: Application to black carbon particles, J. Aerosol Sci., 41, 513–521, https://doi.org/10.1016/j.jaerosci.2010.02.013, 2010.

Peng, J., Hu, M., Guo, S., Du, Z., Zheng, J., Shang, D., Levy Zamora, M., Zeng, L., Shao, M., Wu, Y.-S., Zheng, J., Wang, Y., Glen, C. R., Collins, D. R., Molina, M. J., and Zhang, R.: Markedly enhanced absorption and direct radiative forcing of black carbon under polluted urban environments, P. Natl. Acad. Sci. USA, 113, 4266–4271, https://doi.org/10.1073/pnas.1602310113, 2016.

Petzold, A., Ogren, J. A., Fiebig, M., Laj, P., Li, S.-M., Baltensperger, U., Holzer-Popp, T., Kinne, S., Pappalardo, G., Sugimoto, N., Wehrli, C., Wiedensohler, A., and Zhang, X.-Y.: Recommendations for reporting "black carbon" measurements, Atmos. Chem. Phys., 13, 8365–8379, https://doi.org/10.5194/acp-13-8365-2013, 2013.

Popovicheva, O. B., Chichaeva, M. A., Evangeliou, N., Eckhardt, S., Diapouli, E., and Kasimov, N. S.: Multi-year black carbon observations and modeling close to the largest gas flaring and wildfire regions in the Western Siberian Arctic, Atmos. Chem. Phys., 25, 7719–7739, https://doi.org/10.5194/acp-25-7719-2025, 2025.

Prince, A., Wade, J., Grassian, V., Kleiber, P., and Young, M.: Heterogeneous reactions of soot aerosols with nitrogen dioxide and nitric acid: atmospheric chamber and Knudsen cell studies, Atmos. Environ., 36, 5729–5740, https://doi.org/10.1016/S1352-2310(02)00626-X, 2002.

Riemer, N., West, M., Zaveri, R., and Easter, R.: Estimating black carbon aging time-scales with a particle-resolved aerosol model, J. Aerosol Sci., 41, 143–158, https://doi.org/10.1016/j.jaerosci.2009.08.009, 2010.

Schwarz, J. P., Gao, R. S., Fahey, D. W., Thomson, D. S., Watts, L. A., Wilson, J. C., Reeves, J. M., Darbeheshti, M., Baumgardner, D. G., Kok, G. L., Chung, S. H., Schulz, M., Hendricks, J., Lauer, A., Kärcher, B., Slowik, J. G., Rosenlof, K. H., Thompson, T. L., Langford, A. O., Loewenstein, M., and Aikin, K. C.: Single-particle measurements of midlatitude black carbon and light-scattering aerosols from the boundary layer to the lower stratosphere, J. Geophys. Res.-Atmos., 111, https://doi.org/10.1029/2006JD007076, 2006.

Sedlacek III, A. J., Lewis, E. R., Kleinman, L., Xu, J., and Zhang, Q.: Determination of and evidence for non-core-shell structure of particles containing black carbon using the Single-Particle Soot Photometer (SP2), Geophys. Res. Lett., 39, https://doi.org/10.1029/2012GL050905, 2012.

Song, X.-H., Hopke, P. K., Fergenson, D. P., and Prather, K. A.: Classification of Single Particles Analyzed by ATOFMS Using an Artificial Neural Network, ART-2A, Anal. Chem., 71, 860–865, https://doi.org/10.1021/ac9809682, 1999.

Spencer, M. T. and Prather, K. A.: Using ATOFMS to Determine OC/EC Mass Fractions in Particles, Aerosol Sci. Technol., 40, 585–594, https://doi.org/10.1080/02786820600729138, 2006.

Stephens, M., Turner, N., and Sandberg, J.: Particle identification by laser-induced incandescence in a solid-state laser cavity, Appl. Opt., 42, 3726–3736, https://doi.org/10.1364/AO.42.003726, 2003.

Sun, J. Y., Wu, C., Wu, D., Cheng, C., Li, M., Li, L., Deng, T., Yu, J. Z., Li, Y. J., Zhou, Q., Liang, Y., Sun, T., Song, L., Cheng, P., Yang, W., Pei, C., Chen, Y., Cen, Y., Nian, H., and Zhou, Z.: Amplification of black carbon light absorption induced by atmospheric aging: temporal variation at seasonal and diel scales in urban Guangzhou, Atmos. Chem. Phys., 20, 2445–2470, https://doi.org/10.5194/acp-20-2445-2020, 2020.

Wang, Q., Huang, R., Zhao, Z., Cao, J., Ni, H., Tie, X., Zhu, C., Shen, Z., Wang, M., Dai, W., Han, Y., Zhang, N., and Prévôt, A. S. H.: Effects of photochemical oxidation on the mixing state and light absorption of black carbon in the urban atmosphere of China, Environ. Res. Lett., 12, 044012, https://doi.org/10.1088/1748-9326/aa64ea, 2017.

Wang, Y., Li, W., Huang, J., Liu, L., Pang, Y., He, C., Liu, F., Liu, D., Bi, L., Zhang, X., and Shi, Z.: Nonlinear Enhancement of Radiative Absorption by Black Carbon in Response to Particle Mixing Structure, Geophys. Res. Lett., 48, e2021GL096437, https://doi.org/10.1029/2021GL096437, 2021a.

Wang, Y., Li, W., Huang, J., Liu, L., Pang, Y., He, C., Liu, F., Liu, D., Bi, L., Zhang, X., and Shi, Z.: Nonlinear Enhancement of Radiative Absorption by Black Carbon in Response to Particle Mixing Structure, Geophys. Res. Lett., 48, e2021GL096437, https://doi.org/10.1029/2021GL096437, 2021b.

Wei, J., Niu, Y.-B., Tang, M.-X., Peng, Y., Cao, L.-M., He, L.-Y., and Huang, X.-F.: Characterizing formation mechanisms of secondary aerosols on black carbon in a megacity in South China, Sci. Total Environ., 859, 160290, https://doi.org/10.1016/j.scitotenv.2022.160290, 2023.

Wu, Y., Cheng, T., Liu, D., Allan, J. D., Zheng, L., and Chen, H.: Light Absorption Enhancement of Black Carbon Aerosol Constrained by Particle Morphology, Environ. Sci. Technol., 52, 6912–6919, https://doi.org/10.1021/acs.est.8b00636, 2018.

Xue, L., Gu, R., Wang, T., Wang, X., Saunders, S., Blake, D., Louie, P. K. K., Luk, C. W. Y., Simpson, I., Xu, Z., Wang, Z., Gao, Y., Lee, S., Mellouki, A., and Wang, W.: Oxidative capacity and radical chemistry in the polluted atmosphere of Hong Kong and Pearl River Delta region: analysis of a severe photochemical smog episode, Atmos. Chem. Phys., 16, 9891–9903, https://doi.org/10.5194/acp-16-9891-2016, 2016.

Yang, Z., Ma, N., Wang, Q., Li, G., Pan, X., Dong, W., Zhu, S., Zhang, S., Gao, W., He, Y., Xie, L., Zhang, Y., Kuhn, U., Xu, W., Kuang, Y., Tao, J., Hong, J., Zhou, G., Sun, Y., Su, H., and Cheng, Y.: Characteristics and source apportionment of black carbon aerosol in the North China Plain, Atmos. Res., 276, 106246, https://doi.org/10.1016/j.atmosres.2022.106246, 2022.

Zauscher, M. D., Wang, Y., Moore, M. J. K., Gaston, C. J., and Prather, K. A.: Air Quality Impact and Physicochemical Aging of Biomass Burning Aerosols during the 2007 San Diego Wildfires, Environ. Sci. Technol., 47, 7633–7643, https://doi.org/10.1021/es4004137, 2013.

Zhai, J., Yang, X., Li, L., Bai, B., Liu, P., Huang, Y., Fu, T.-M., Zhu, L., Zeng, Z., Tao, S., Lu, X., Ye, X., Wang, X., Wang, L., and Chen, J.: Absorption Enhancement of Black Carbon Aerosols Constrained by Mixing-State Heterogeneity, Environ. Sci. Technol., 56, 1586–1593, https://doi.org/10.1021/acs.est.1c06180, 2022a.

Zhai, J., Yang, X., Li, L., Ye, X., Chen, J., Fu, T., Zhu, L., Shen, H., Ye, J., Wang, C., and Tao, S.: Direct Observation of the Transitional Stage of Mixing-State-Related Absorption Enhancement for Atmospheric Black Carbon, Geophys. Res. Lett., 49, e2022GL101368, https://doi.org/10.1029/2022GL101368, 2022b.

Zhai, J., Shao, S., Yang, X., Zeng, Y., Fu, T.-M., Zhu, L., Shen, H., Ye, J., Wang, C., and Tao, S.: Chemically Resolved Respiratory Deposition of Ultrafine Particles Characterized by Number Concentration in the Urban Atmosphere, Environ. Sci. Technol., 58, 16507–16516, https://doi.org/10.1021/acs.est.4c03279, 2023.

Zhai, J., Zhang, Y., Liu, P., Zhang, Y., Zhang, A., Zeng, Y., Cai, B., Zhang, J., Xing, C., Yang, H., Wang, X., Ye, J., Wang, C., Fu, T.-M., Zhu, L., Shen, H., Tao, S., and Yang, X.: Source-dependent optical properties and molecular characteristics of atmospheric brown carbon, Atmos. Chem. Phys., 25, 7959–7972, https://doi.org/10.5194/acp-25-7959-2025, 2025.

Zhang, G., Fu, Y., Peng, X., Sun, W., Shi, Z., Song, W., Hu, W., Chen, D., Lian, X., Li, L., Tang, M., Wang, X., and Bi, X.: Black Carbon Involved Photochemistry Enhances the Formation of Sulfate in the Ambient Atmosphere: Evidence From In Situ Individual Particle Investigation, J. Geophys. Res.-Atmos., 126, e2021JD035226, https://doi.org/10.1029/2021JD035226, 2021.

Zhang, R., Khalizov, A. F., Pagels, J., Zhang, D., Xue, H., and McMurry, P. H.: Variability in morphology, hygroscopicity, and optical properties of soot aerosols during atmospheric processing, P. Natl. Acad. Sci. USA, 105, 10291–10296, https://doi.org/10.1073/pnas.0804860105, 2008.

Zhang, Y.: Dataset for Zhang2026_ACP [Dataset]. In Contrasting Nighttime Heterogeneous and Daytime Photochemical Aging Drive the Optical Evolution of Black Carbon, Zenodo [data set], https://doi.org/10.5281/zenodo.21973372, 2026.

Zhang, Y., Zhang, Q., Cheng, Y., Su, H., Li, H., Li, M., Zhang, X., Ding, A., and He, K.: Amplification of light absorption of black carbon associated with air pollution, Atmos. Chem. Phys., 18, 9879–9896, https://doi.org/10.5194/acp-18-9879-2018, 2018.

Zhang, Y., Wang, J., Wu, N., Ouyang, X., Li, G., Cheng, Y., Zhang, Q., Ding, A., and Su, H.: The Contribution of Black Carbon Containing Particles to $PM_{2.5}$: Variability, Drivers, and Impacts, Environ. Sci. Technol., 59, 5155–5163, https://doi.org/10.1021/acs.est.5c00675, 2025.

Zhou, Q., Cheng, C., Yang, S., Yuan, M., Meng, J., Gong, H., Zhong, Q., Zhang, Y., Xie, Y., Zhou, Z., and Li, M.: Enhanced mixing state of black carbon with nitrate in single particles during haze periods in Zhengzhou, China, J. Environ. Sci., 111, 185–196, https://doi.org/10.1016/j.jes.2021.03.031, 2022.